Sustainable Energy & Fuels

# Interface engineering for light-driven water oxidation: Unravelling the passivating and catalytic mechanism in $BiVO_4$ overlayers

| | |
|---|---|
| Journal: | *Sustainable Energy & Fuels* |
| Manuscript ID | SE-ART-09-2018-000473.R1 |
| Article Type: | Paper |
| Date Submitted by the Author: | 11-Oct-2018 |
| Complete List of Authors: | Liu, Guiji; Lawrence Berkeley National Lab, Joint center for Artificial Photosynthesis<br>Eichhorn, Johanna; Lawrence Berkeley National Laboratory, Advanced Light Srouce<br>Jiang, Chang-Ming; Technische Universitat Munchen Physik-Department,<br>Scott, Mary; Molecular Foundry at Lawrence Berkeley National Laboratory,<br>Hess, Lucas; Lawrence Berkeley National Lab, JCAP<br>Gregoire, John; California Institute of Technology, Joint Center for Artificial Photosynthesis<br>Haber, Joel; California Institute of Technology, Joint Center for Artificial Photosynthesis<br>Sharp, Ian; Lawrence Berkeley National Laboratory, JCAP; Lawrence Berkeley National Laboratory, Chemical Sciences Division; Technische Universiat Munchen, Walter Schottky Institut and Physik Department<br>Toma, Francesca Maria; Lawrence Berkeley National Lab, Joint center for Artificial Photosynthesis |
| | |

Journal Name

ARTICLE

# Interface engineering for light-driven water oxidation: Unravelling the passivating and catalytic mechanism in $BiVO_4$ overlayers †

Guiji Liu,[a,b] Johanna Eichhorn,[a,b] Chang-Ming Jiang,[a,b] Mary C. Scott,[e,f] Lucas H. Hess,[a,b] John M. Gregoire,[c] Joel A. Haber,[c] Ian D. Sharp,[a,b,d] and Francesca M. Toma,* [a,b]

Received 00th January 20xx,
Accepted 00th January 20xx

DOI: 10.1039/x0xx00000x

**www.rsc.org/**

Artificial photosynthetic approaches require the combination of light absorbers interfaced with overlayers that enhance charge transport and collection to perform catalytic reactions. Despite numerous efforts that have coupled various catalysts to light absorbing semiconductors, the optimization of semiconductor/catalyst as well as catalyst/electrolyte interfaces and the identification of the role of the catalyst still remain a key challenge. Herein, we assemble $(NiFeCoCe)O_x$ multi-component overlayers, interfaced with bismuth vanadate photoanodes, and determine the roles of different elements on promoting interfacial charge transfer and catalytic reaction over competitive photocarrier recombination loss processes. Through this understanding, and aided by complementary macroscopic photoelectrochemical measurements and nanoscale atomic force microscopy techiniques, a bifunctional $(CoFeCe/NiFe)O_x$ overlayer was rationally engineered. The resuting multi-functional coating yields $BiVO_4$ photoanodes with almost 100% efficient surface collection of holes under oxygen evolving reaction conditions. The $(CoFeCe)O_x$ component excels at efficient capture and transport of photogenerated holes in $BiVO_4$ through the availability of redox active states, whereas $(NiFe)O_x$ plays a vital role in reducing charge recombination at the $BiVO_4$/electrolyte interface. In addition, this study supports the hypothesis that catalytic sites act as electronically active trap states on uncoated $BiVO_4$ photoanodes.

## 1. Introduction

The adverse effect of intensive fossil fuel usage on our environment has motivated the search for clean and renewable energy technologies. However, for many of these technologies, energy storage still remains a limiting factor.[1] By converting the large but intermittent solar energy flux into chemical fuels, artificial photosynthesis holds promise to overcome this challenge and provide a sustained energy supply for our societal needs.[2, 3] Photoelectrochemical (PEC) water splitting and $CO_2$ reduction represent intriguing routes to produce clean fuels using sunlight.[4-7] As the electrons and protons needed for solar fuels production hinge on the oxidation of water, an efficient photoanode is a prerequisite for a viable solar fuels technology.

Among promising semiconductor photoanode materials, bismuth vanadate ($BiVO_4$) has emerged as one of the most investigated systems in unassisted water-splitting devices, as it captures a substantial portion of the visible spectrum and possesses band energetics that are well-suited for the oxygen evolution reaction (OER).[8] However, the bare surface of this material suffers from poor catalytic activity for the OER and possesses high concentrations of electronically active surface states, leading to significant charge recombination losses[9, 10] and corrosion.[11] Numerous studies have demonstrated that $BiVO_4$ needs to be paired with catalysts to achieve suitable photocurrents for OER.[12-19] However, different working mechanisms have been reported for these catalysts, depending on the physicochemical nature of the $BiVO_4$/catalyst interface. For example, Durrant, et al. concluded that the origin of the enhanced photocurrent resulting from cobalt phosphate (CoPi) catalyst treatment is primarily due to improved charge transfer across the $BiVO_4$/electrolyte interface rather than the catalytic function of CoPi,.[19] This argument was strengthened by a recent report of Van de Krol, et al., which highlights that CoPi passivates the surface states of $BiVO_4$ without significantly influencing the charge transfer kinetics.[20] On the other hand, Gamelin and co-workers came to a different conclusion that CoPi promoted charge transfer for OER,

---

[a] Joint Center for Artificial Photosynthesis, Lawrence Berkeley National Laboratory, 1 Cyclotron Road, Berkeley, California 94720, USA.
[b] Chemical Sciences Division, Lawrence Berkeley National Laboratory, 1 Cyclotron Road, Berkeley, California 94720, USA.
[c] Joint Center for Artificial Photosynthesis, California Institute of Technology; Pasadena, CA 91125, USA.
[d] Walter Schottky Institut and Physik Department, Technische Universität München, Am Coulombwall 4, 85748 Garching, Germany.
[e] Department of Materials Science and Engineering, University of California Berkeley, Berkeley, USA.
[f] National Center for Electron Microscopy, Molecular Foundry, Lawrence Berkeley National Laboratory, Berkeley, USA
Email: fmtoma@lbl.gov

† Electronic Supplementary Information (ESI) available: See DOI: 10.1039/x0xx00000x

comparing with $H_2O_2$ as a hole scavenger.[13] In addition, Li, et al., argued that cobalt borate (CoBi) catalyst accelerates interfacial charge transfer at the $BiVO_4$/electrolyte interface.[14] Choi, et al., demonstrated that a FeOOH overlayer creates a favorable interface with $BiVO_4$ as well as acts as an OER catalyst.[15]

The different interpretations of the improvement mechanisms for the proposed overlayers highlight the variety of demands placed on the catalyst coating, as well as the challenge in discerning the prominent function(s) due to the confluence of these phenomena during photoelectrochemical reactions. Specifically, a good catalyst layer deposited on a light absorber needs to out-compete surface states in capturing holes in order to be efficient for OER catalysis. The rate of these competing kinetic pathways determines whether the passivation mechanism will dominate over the catalytic one or vice versa. Disentangling the respective passivation and catalytic roles of light absorber overlayers is currently needed to provide the necessary insight for further development of highly efficient and stable integrated photoanodes. In order to address this issue, multi-component overlayers with complimentary hole transport and catalytic functions are practically required. While a few examples of multi-component catalytic layers have been reported to improve the efficiency of $BiVO_4$,[16, 17] the charge transfer and collection mechanism in these overlayers still remains unclear.

Here, *via* an individual component analysis, we rationally design $(NiFeCoCe)O_x$ multi-component coatings on $BiVO_4$ photoanodes to investigate how the specific properties of the light absorber/catalyst interface define the interfacial charge transfer and collection mechanism, as well as to simultaneously optimize the passivating and catalytic functions. Based on our high-throughput direct discovery of $BiVO_4$/multi-component functional interfaces,[18, 19] we deposit $(NiFeCoCe)O_x$ multi-component overlayers by photoelectrochemical deposition (PED). PED is a straightforward method that is well suited for producing diverse compositions of coatings and creating interfacial structures with $BiVO_4$.[21] In addition, PED inherently places catalysts at the specific locations of the $BiVO_4$/electrolyte interface where the photogenerated holes are most readily available without coating the underlying FTO.[15] However, to the best of our knowledge, attempts to deposit controlled multi-element compositions by this versatile technique are rare.[21]

To clarify the role of the different components and enable the rational design of a targeted multi-component overlayer, we studied individual (Ni, Fe, Co, Ce) oxides in multi-component (NiFe, CoFeCe, and CoFeCe/NiFe) oxide components. Thus, we demonstrate that an optimized light absorber/overlayer interface necessitates a dual hole transport/catalyst coating. We combined a suite of photoelectrochemical (PEC) and microscopy techniques to characterize the nanoscale distribution and functionality of the catalyst on the photoanode surface. Thus, we correlate this information with macroscopic PEC measurements to provide deeper understanding of charge transfer at the light absorber/overlayer interface. Analysis of the role of the individual overlayer components shows that while $CeO_x$ is excellent at passivating active surface states, it reduces the $BiVO_4$ catalytic activity under OER conditions. Specifically, the $CeO_x$ overlayer produces discontinuous films that together with the photoelectrochemical findings support that surface trap states in $BiVO_4$ may be responsible for OER catalysis. In addition, using PEC characterization we identify $(NiFe)O_x$ as the most active surface catalyst, and $(CoFeCe)O_x$ as an interfacial charge transfer and collection layer in $(NiFeCoCe)O_x$ multi-component coatings. Furthermore, we investigate the interface energetics and dynamics of multi-component $BiVO_4/(CoFeCe)O_x$ by open circuit potential (OCP) and transient photocurrent (TPC) measurements. These measurements demonstrate that $(CoFeCe)O_x$ is able to extract and collect holes from $BiVO_4$ by introducing surface redox states for OER. Based on the understanding of $(NiFeCoCe)O_x$, we optimize the $BiVO_4$/overlayer interface by sequentially integrating $(CoFeCe)O_x$ as a hole transport and collecting layer and $(NiFe)O_x$ as a surface catalyst with $BiVO_4$. The resulting photoanode achieved near-complete suppression of interface losses between 0.8 and 1.23 V vs. reverse hydrogen electrode (RHE) for solar water oxidation. In addition, we utilize atomic force microscopy (AFM) to discern and map the overlayer morphology on top of the $BiVO_4$ photoanode and provide subsequent insights with photoconductive AFM (pc-AFM) measurements to reveal that the holes collected by $(CoFeCe)O_x$ can be efficiently used by $(NiFe)O_x$ for water oxidation. These findings shed light on interface engineering and optimization with $BiVO_4$/catalyst assemblies, thereby offering guidelines to accelerate discovery of functional components for PEC water splitting devices.

## 2. Results and discussion

In the present work, spin-coated, undoped $BiVO_4$ thin films on fluorine doped tin oxide (FTO)/glass substrates were prepared as previously reported.[11] As a starting point for understanding the properties of $BiVO_4/(NiFeCoCe)O_x$ multi-component overlayers, we investigate the specific role of Ni, Fe, Co and Ce by individually depositing each overlayer component ($NiO_x$, $FeO_x$, $CoO_x$ and $CeO_x$) on $BiVO_4$ films with PED under constant current density. J-E measurements in 0.1 M NaOH solution with and without $H_2O_2$ as a hole scavenger were conducted (Fig. 1a and b). Measurements with $H_2O_2$ hole scavenger are performed to minimize recombination losses associated with slow catalytic processes and assess the quality of the semiconductor/overlayer assembly for capturing light and separating/transporting charge. In the absence of $H_2O_2$, the measured photocurrent is lower due to the significant competition between the sluggish kinetics of OER and surface recombination.

The J-E curves in the presence of $H_2O_2$ (Fig. 1a) show onset potentials at 0.4 V vs. RHE for $BiVO_4/NiO_x$, $BiVO_4/FeO_x$, $BiVO_4/CeO_x$ and pristine $BiVO_4$ photoanodes. $FeO_x$ shows slightly more favourable onset characteristics at 0.4-0.8 V vs. RHE. As the

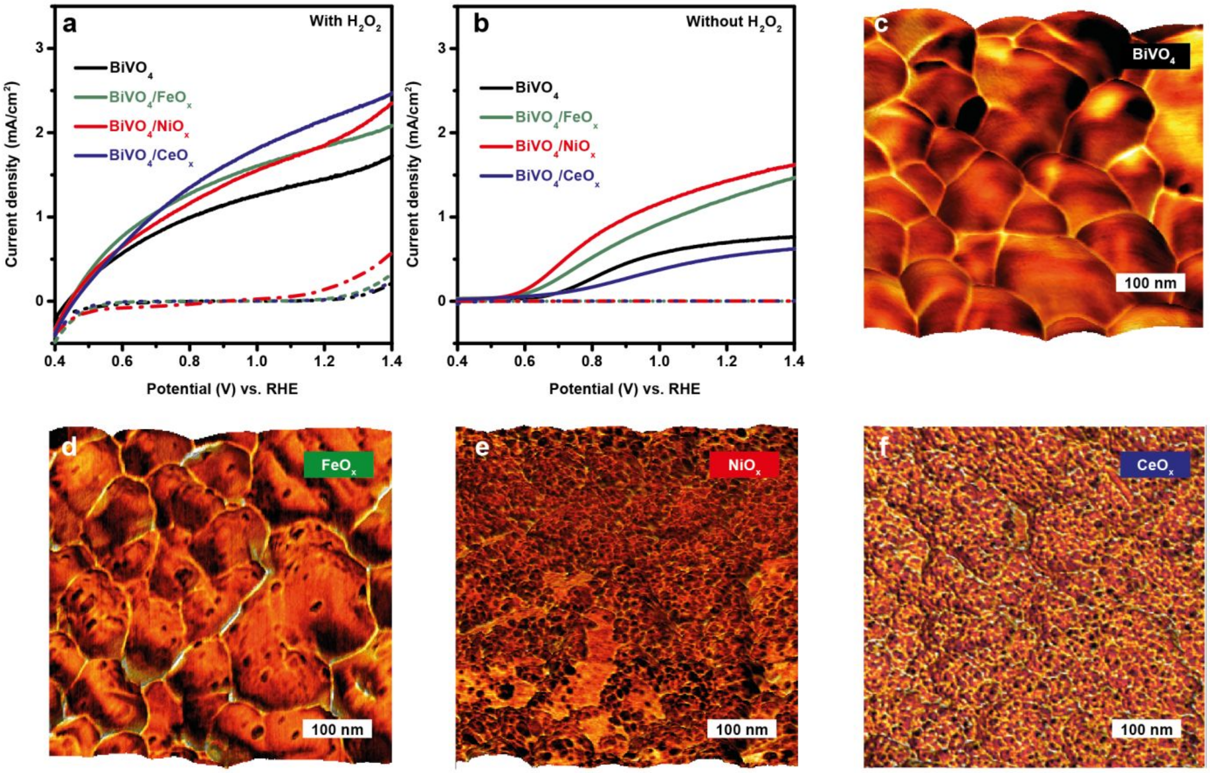

**Figure 1 PEC and AFM characteristics of individual catalyst components.** Current-potential curves of $BiVO_4$, $BiVO_4/NiO_x$, $BiVO_4/FeO_x$, and $BiVO_4/CeO_x$ photoanodes in dark (dashed lines) and under AM 1.5G simulated sunlight at 100 mW $cm^{-2}$ (solid lines) in **a)** 0.1 M NaOH + $H_2O_2$ aqueous solution (pH = 13) and **b)** 0.1 M NaOH aqueous solution (pH = 13). Overlay images of the sample topography and the corresponding adhesion maps for **c)** $BiVO_4$, **d)** $BiVO_4/FeO_x$, **e)** $BiVO_4/NiO_x$ and **f)** $BiVO_4/CeO_x$.

applied potential increases, the corresponding photocurrent densities of all samples increase rapidly, as expected since charge extraction is a function of the applied potential. The pristine $BiVO_4$ photoanode exhibits a photocurrent density of 1.5 mA $cm^{-2}$ at 1.23 V vs. RHE, whereas $BiVO_4/NiO_x$, $BiVO_4/FeO_x$, and $BiVO_4/CeO_x$ show about 1.9, 1.9, and 2.2 mA $cm^{-2}$, respectively, at the same potential. Unexpectedly, while $CeO_x$ is not catalytically active for OER,[22] $BiVO_4/CeO_x$ exhibits the highest photocurrent density in the presence of $H_2O_2$ at 0.8-1.4 V vs. RHE. The enhanced performance of $BiVO_4$ upon different overlayers may be attributed to improved light absorption or charge separation/transport. According to UV-Vis measurements, the addition of overlayers with PED barely alters light absorption of $BiVO_4$ (Fig. S1). Moreover, all samples exhibit similar onset potential (~0.4 V vs. RHE) in Fig. 1a, thus implying a similar interfacial energetics for driving charge separation.

Therefore, the enhanced performances of $BiVO_4/NiO_x$, $BiVO_4/FeO_x$, and $BiVO_4/CeO_x$ with $H_2O_2$ may be ascribed to the facilitated charge transport by passivating intrinsic surface states of $BiVO_4$. Specifically, $CeO_x$ is the most effective at passivating surface states at high potential region, and $FeO_x$ is excellent at passivating surface states at the onset region. These observations agree well with previous reports on the excellent interface properties of $BiVO_4/FeO_x$[16] and $BiVO_4/CeO_x$.[23]

By comparing the photocurrents for water and $H_2O_2$ oxidation, we can examine the surface hole injection efficiencies in $BiVO_4$/catalyst assemblies as $P_{hole\ injection} = J^{H2O}/J^{H2O2}$. The corresponding J-E curves of $NiO_x$, $FeO_x$, and $CeO_x$ loaded $BiVO_4$ photoanodes without $H_2O_2$ are shown in Fig. 1b. $BiVO_4/NiO_x$ and $BiVO_4/FeO_x$ exhibit an enhanced photocurrent density at 1.23 V vs. RHE (1.3 and 1.5 mA $cm^{-2}$) with respect to bare $BiVO_4$ (0.7 mA $cm^{-2}$). However, relative to the pristine $BiVO_4$, the $BiVO_4/CeO_x$ assembly shows a significantly reduced photocurrent density for water oxidation over the entire operating potential range. This result contrasts sharply with the superior performance of $BiVO_4/CeO_x$ in the presence of $H_2O_2$, (Fig. 1a), thus confirming that the catalytic activity of $CeO_x$ for OER is very poor. Thus, a large portion of holes that reach the surface tend to undergo recombination instead of interfacial charge transfer, despite the favourable properties of $CeO_x$ for passivating electronically active surface defects.

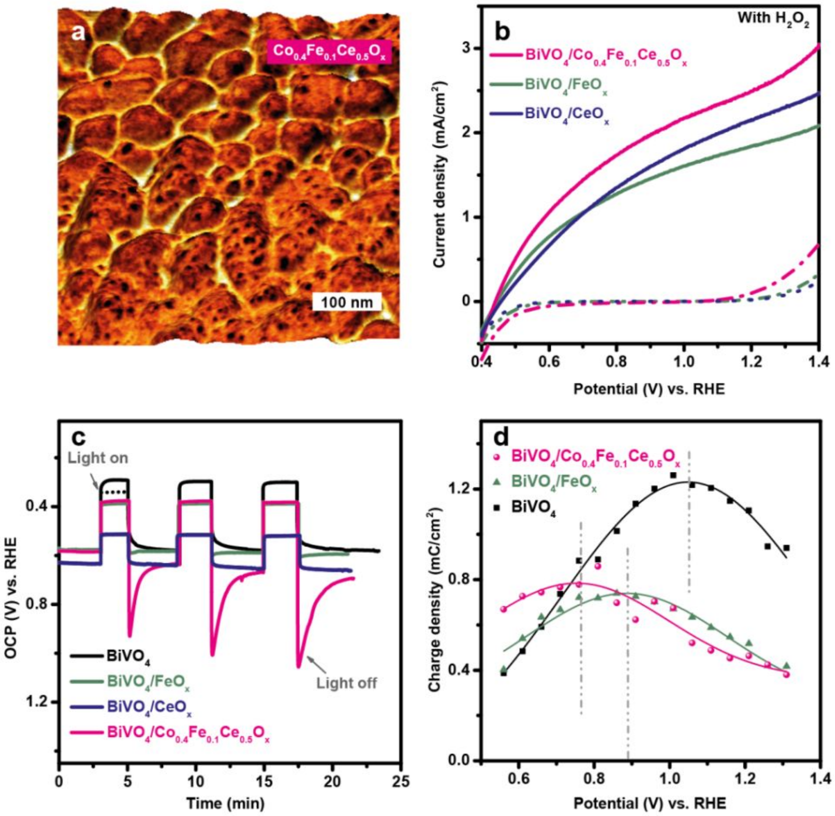

**Figure 2 Characterizations of (CoFeCe)$O_x$ overlayer. a)** Overlay images of the sample topography and the corresponding adhesion maps for $BiVO_4/Co_{0.4}Fe_{0.1}Ce_{0.5}O_x$, **b)** Current-potential curves of $BiVO_4/FeO_x$, $BiVO_4/CeO_x$and $BiVO_4/Co_{0.4}Fe_{0.1}Ce_{0.5}O_x$ photoanodes in dark (dashed lines) and under AM 1.5G simulated sunlight at 100 mW $cm^{-2}$ in 0.1 M NaOH + $H_2O_2$ aqueous solution (pH = 13). **c)** OCP values of pristine $BiVO_4$, $BiVO_4/FeO_x$, $BiVO_4/CeO_x$ and $BiVO_4/Co_{0.4}Fe_{0.1}Ce_{0.5}O_x$ photoanodes in 0.1 M NaOH solution at pH 13 under chopped illumination. The upper right inset shows an enlarged view of region within the dashed square. **d)** Accumulated charge versus potential curves obtained from transient photocurrent data of $BiVO_4$, $BiVO_4/FeO_x$, $BiVO_4/CeO_x$ and $BiVO_4/Co_{0.4}Fe_{0.1}Ce_{0.5}O_x$ photoanodes collected in 0.1 M NaOH solution at pH 13 under background white light bias at 1 sun intensity.

In order to estimate the probability that holes reaching the $BiVO_4$ surface can effectively contribute to OER, the hole injection efficiency at 1.23 V vs. RHE was calculated for these $BiVO_4$/catalyst assemblies (Table S1). For pristine $BiVO_4$, the hole injection efficiency is only 48% at 1.23 V vs. RHE. This finding reveals significant kinetic competition between surface recombination and water oxidation, which is in line with previous reports.[14, 15] Once coupled with $NiO_x$ or $FeO_x$, this value goes up to 79% or 67%, respectively. This result is in good agreement with the enhanced photocurrent with respect to pristine $BiVO_4$ in Fig. 1b, thereby implying that both $NiO_x$ and $FeO_x$ retain $BiVO_4$ catalytic activity and introduce catalytic sites for OER onto $BiVO_4$ surfaces. However, $CeO_x$ results in a hole injection efficiency of 27% at 1.23 V vs. RHE. Thus, $CeO_x$ appears to dramatically reduce overall catalytic activity of the photoelectrode, presumably due to coating the moderately active semiconductor surface with a more chemically inert material, $CeO_x$.

In order to better understand the role of each individual component, we analysed the morphology and nanomechanical adhesion properties of the overlayer with atomic force microscopy (AFM). This technique allows for direct visualization of the distribution of different oxide overlayers nanoparticles on the $BiVO_4$ semiconductor. Specifically, we use the topography images overlayed by the corresponding adhesion maps to provide nanoscale information on the surface structure of the $BiVO_4$/overlayer assembly. Fig. 1c-f show the overlay images for bare $BiVO_4$, $BiVO_4/FeO_x$, $BiVO_4/NiO_x$, and $BiVO_4/CeO_x$, respectively. The pristine $BiVO_4$ film exhibits individual $BiVO_4$ grains ranging between 50 and 200 nm in size with an overall smooth surface. After depositing $FeO_x$, $NiO_x$ and $CeO_x$, it is possible to identify 5-10 nm nanoparticles dispersed on the surfaces of $BiVO_4$ grains with different degrees of coverage. Specifically, it is interesting to notice that $CeO_x$ particles are homogenously yet discontinuously dispersed on top of the $BiVO_4$ light absorber (Fig. 1f). This morphology together with the PEC measurements support that while $CeO_x$ passivates electronically active trap states in $BiVO_4$, it also reduces catalytically active states. Consequently, this finding leads us to conclude that the surface trap states may be the catalytic states of bare $BiVO_4$, thus explaining why the $BiVO_4/CeO_x$ shows reduced catalytic activity towards OER.

In contrast to $NiO_x$, $FeO_x$, and $CeO_x$,, $CoO_x$ did not show a significant photoresponse under either front or back-side illumination but greatly enhanced dark current for OER (Fig. S2a). It should also be noted that $CoO_x$ was only deposited for 5 min, as the potential required for deposition increased sharply (Fig. S2b), whereas the standard deposition time for all other samples was 60 min. This modified deposition approach avoided massive growth of $CoO_x$ on $BiVO_4$, and prevented $CoO_x$ from affecting light absorption of $BiVO_4$ (Fig. S2c). $CoO_x$ deposition eliminates the built-in potential and, thus, the driving force for photocarrier separation. A similar phenomenon was observed for the case of $IrO_x$ on $WO_3$, which yields an ohmic solid/solid contact.[24] This conclusion explains the observation that the $BiVO_4/CoO_x$ anode behaves like a conducting electrocatalyst for OER. Thus, the $BiVO_4/CoO_x$ junction energetics are poorly suited for creating efficient photoelectrodes.

Based on the above PEC characterization and the charge injection efficiency values of the individual overlayer components, we summarized individual role of the metal oxide overlayers in Fig. S3. It is clear that $NiO_x$ is the main catalytic component in the $(NiFeCoCe)O_x$ multi-component coatings. On the other hand, $CeO_x$ and $CoO_x$ modify the interfacial properties of $BiVO_4$, by passivating electronically active trap states and decreasing the built in potential, respectively. In addition, $FeO_x$ has moderate impact on both catalytic and passivating functions. Based on these insights, we rationally designed, synthesized, and tested a multi-layer coating with the aim of optimizing both the semiconductor/overlayer interface and the catalytic activity. To this end, we modified $NiO_x$ with $FeO_x$ to form a $Ni_{0.8}Fe_{0.2}O_x$ catalytic layer at the outer surface by PED using mixed 0.08 M nickel (II) nitrate hexahydrate, 0.02 M iron nitrate (III) nonahydrate as plating solution, which provides superior catalytic activity relative to the pure $NiO_x$ or $FeO_x$ (Fig. S4). Given the beneficial interface of $BiVO_4/FeO_x$ and $BiVO_4/CeO_x$, we attempted to combine $FeO_x$ and $CeO_x$ into an interface layer for efficiently collecting holes over the entire operating potential range. However, the combination of Fe and Ce species results in poor coating of $BiVO_4$ with PED, which greatly limits the performance of $BiVO_4/(FeCe)O_x$ (Fig S5a and c). The different morphologies of $CeO_x$ and $(FeCe)O_x$ indicate that the interaction between Fe and Ce species leads to a different growth process of the ternary oxide, as supported by the enlarged potential for depositing $(FeCe)O_x$ (Fig. S5b). Interestingly, we found that incorporating 80% of Co into (FeCe) precursor solution not only leads to uniform coating of $(CoFeCe)O_x$ on $BiVO_4$ with PED but also offers additional redox active sites that are available for hole collection and transport, as demonstrated below. X-ray photoelectron spectroscopy (XPS) measurements revealed that the deposited $(CoFeCe)O_x$ consists of $Co^{(II/III)}$, $Fe^{(III)}$ and $Ce^{(III/IV)}$ in the form of oxyhydroxides (Fig S6). Since XPS is a surface sensitive technique, Inductively coupled plasma mass spectrometry (ICP-MS) was used for complementary analysis of the overall composition of $(CoFeCe)O_x$. The ICP-MS results reveal that the $(CoFeCe)O_x$ is composed of Co: 40%, Fe: 10% and Ce: 50% ($Co_{0.4}Fe_{0.1}Ce_{0.5}O_x$), thus indicating a preferential deposition of $CeO_x$ on $BiVO_4$ during PED. In addition, energy-dispersive X-ray spectroscopy (EDX) maps, obtained on scanning transmission electron microscopy images (STEM), highlight the presence of the overlayer atop the $BiVO_4$ (Fig. S7), which shows uniform coating on $BiVO_4$ (Fig. 2a). As a result, $BiVO_4/Co_{0.4}Fe_{0.1}Ce_{0.5}O_x$ shows a superior onset characteristics as well as an optimal photocurrent density of 2.4 mA cm$^{-2}$ at 1.23 V vs. RHE with $H_2O_2$, which is higher than $BiVO_4/CeO_x$ (2.2 mA cm$^{-2}$), $BiVO_4/FeO_x$ (1.9 mA cm$^{-2}$) or $BiVO_4/(FeCe)O_x$(1.2 mA cm$^{-2}$) (Fig. S5a) demonstrating that the $BiVO_4/Co_{0.4}Fe_{0.1}Ce_{0.5}O_x$ interface is excellent for transporting holes.

To investigate the interface energetics of the $Co_{0.4}Fe_{0.1}Ce_{0.5}O_x$ layer, we monitored the open circuit potential (OCP) profiles and the charge carrier dynamics by transient photocurrent (TCP) measurements (Fig. 2c and d). For a photoelectrode, changes of OCP reflect charge migration driven by the internal energetics at the electrode/electrolyte interface.[17] As shown in Fig. 2c, the OCP of the pristine $BiVO_4$ photoanode in darkness is at 0.6 V vs. RHE. Under illumination, the OCP of $BiVO_4$ immediately reached an initial value (black dashed line), which further increased over time. This effect indicates that holes are accumulating on the surface under illumination, which can be ascribed to the saturation of surface states by photo-induced processes, analogous to the recently reported photocharging effect on $BiVO_4$.[25] Upon addition of $CeO_x$, OCP of $BiVO_4$ shifts positively, which indicates the physical passivation effect of $CeO_x$ on partially removing surface states of $BiVO_4$, in line with previous findings.[23] In contrast, the addition of $FeO_x$, or $Co_{0.4}Fe_{0.1}Ce_{0.5}O_x$ marginally alters the resting potential of $BiVO_4$ under dark conditions, suggesting that these overlayers provides marginal physical passivation of intrinsic surface states on $BiVO_4$. However, photocharging processes of $BiVO_4$ disappear upon overlayer loading, which indicates those overlayers may offer alternative paths for hole transfer other than through the intrinsic surface states, therefore functionally passivating surface states of $BiVO_4$. This finding can be further supported by the different transient OCPs upon switching off the light. When light is switched off, the OCP of $BiVO_4$ slowly decays to the same position in dark. This slow process reveals that photogenerated holes originally accumulated on the surface of $BiVO_4$ under illumination and charge recombination with majority electrons is required to re-establish equilibrium when illumination is stopped. In contrast, after depositing $CeO_x$ atop, the OCP of $BiVO_4/CeO_x$ goes back to the same position as in dark without an apparent decay process within the time scales detectable with our measurement. The absence of a decay process further supports the passivation effect of $CeO_x$, as mentioned earlier. When light is turned off, we observe a different behaviour with $FeO_x$ and

$Co_{0.4}Fe_{0.1}Ce_{0.5}O_x$. Specifically, the OCP of $BiVO_4/FeO_x$ immediately jumps to a new value, which is 10 mV higher than the initial dark equilibrium value and shows an "opposite" charge recombination decay, compared to the pristine $BiVO_4$. This phenomenon is even more pronounced with $Co_{0.4}Fe_{0.1}Ce_{0.5}O_x$. The OCP of $BiVO_4/Co_{0.4}Fe_{0.1}Ce_{0.5}O_x$ jumps to a position which is 300 mV higher than the initial dark equilibrium value and the "opposite" charge recombination decay for $BiVO_4/Co_{0.4}Fe_{0.1}Ce_{0.5}O_x$ is much more significant than that for $BiVO_4/FeO_x$. The presence of an offset with respect to the initial dark equilibrium suggests that there might be a change in the oxidation state of $FeO_x$ and $Co_{0.4}Fe_{0.1}Ce_{0.5}O_x$ layers, compatible with the presence of photogenerated holes of $BiVO_4$. In other words, this finding proves that $FeO_x$ and $Co_{0.4}Fe_{0.1}Ce_{0.5}O_x$ can extract and collect photogenerated holes from $BiVO_4$ under illumination, building up positively charged species, thereby establishing a new interfacial energetic alignment. The behavior of the $Co_{0.4}Fe_{0.1}Ce_{0.5}O_x$ overlayer implies that the hole extraction ability mainly results from Co species. Indeed, in the absence of Co, the OCP profile of $(FeCe)O_x$ shows no apparent charge recombination decay upon switching off light (Fig.S8), which further demonstrates the important role of Co redox active species in extracting holes from $BiVO_4$. Notably, $BiVO_4/Co_{0.4}Fe_{0.1}Ce_{0.5}O_x$ is exposed to light for only 3 min and requires about 60 min to recover the original resting level of OCP in the dark (Fig. S9). These results indicate that hole extraction and collection from $BiVO_4$ into $Co_{0.4}Fe_{0.1}Ce_{0.5}O_x$ is energetically favourable.

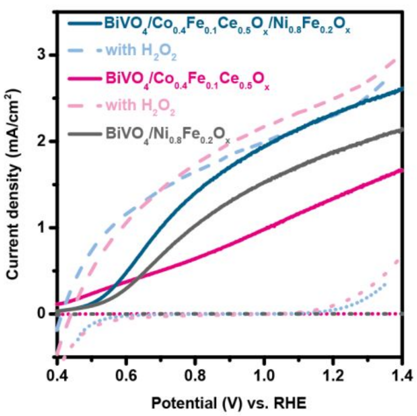

**Figure 3 The PEC characterizations of the (NiFeCoCe)$O_x$ integrated $BiVO_4$ photoanodes.** Current-potential curves of $BiVO_4/Ni_{0.8}Fe_{0.2}O_x$, $BiVO_4/Co_{0.4}Fe_{0.1}Ce_{0.5}O_x$, and $BiVO_4/Co_{0.4}Fe_{0.1}Ce_{0.5}O_x/Ni_{0.8}Fe_{0.2}O_x$ photoanodes in dark (dotted lines) under AM 1.5G simulated sunlight at 100 mW cm$^{-2}$ photoandes in 0.1 M NaOH aqueous solution (pH = 13), comparing to current-potential curves of $BiVO_4/Co_{0.4}Fe_{0.1}Ce_{0.5}O_x/Ni_{0.8}Fe_{0.2}O_x$ and $BiVO_4/Co_{0.4}Fe_{0.1}Ce_{0.5}O_x$ photoanodes (dashed lines) in 0.1 M NaOH + $H_2O_2$ aqueous solution (pH = 13).

To gain more insight into the charge carrier dynamics between $(CoFeCe)O_x$ and $BiVO_4$ under operating conditions, TPC measurements were employed using a pulsed 340 nm LED and a continuous white light source. The photocurrent transients upon light perturbation are indicative of capacitive charge accumulation, which offers the possibility for electrons to recombine. The number of charges accumulated at the electrode/electrolyte interface can be qualitatively determined by integrating the photocurrent transients during the monitored surface recombination process. The potential peaks of the accumulation maximum most probably represent the energy levels of surface redox states, which shed light on the interfacial charge capture/collection on $BiVO_4$ surfaces.[26-28] To depict this clearly, a plot of the accumulated charge versus potential is shown in Fig. 2d, which is obtained by integrating the photocurrent transients measured in Fig. S10. Pristine $BiVO_4$ shows the most pronounced charge accumulation at the electrode/electrolyte interface. When covering the $BiVO_4$ photoanode surface with overlayers, charge accumulation is attenuated and occurs at more cathodic potentials. The cathodic shift provides strong evidence that the overlayers out-compete the intrinsic surface states for capturing holes, thus providing alternative paths for hole transfer. In particular, the addition of $FeO_x$ cathodically shifts the maximum charge accumulation, indicating that the Fe redox states have more driving force to capture and accumulate holes over the intrinsic surface states on $BiVO_4$. In contrast, almost no charge accumulation can be calculated from TPC results of $BiVO_4/CeO_x$ (Fig. S10c), once again, confirming the passivation effect that prevents hole accumulation via surface states. Interestingly, adding Ce into $FeO_x$ leads to a great reduction in magnitude of charge accumulation, further indicating that Ce contributes to removing surface states (Fig. S11). These measurements, together with the OCP results, revealed the role of $CeO_x$ in passivating surface states of $BiVO_4$ and creating a favourable interface for hole transport, consistent with our previous study on the $BiVO_4/CeO_x$ interface.[23] Moreover, a further shift in the energy levels of redox states to 0.7 V vs. RHE is observed due to the presence of $Co_{0.4}Fe_{0.1}Ce_{0.5}O_x$. This finding suggests that Co offers additional redox states for accepting surface holes. Interestingly, CV measurements of $BiVO_4/Co_{0.4}Fe_{0.1}Ce_{0.5}O_x$ in the dark also show redox features at 0.7 V vs. RHE, produced by Co and Fe species (Fig. S12). Given the findings above, it is very likely that $Co_{0.4}Fe_{0.1}Ce_{0.5}O_x$ acts as an interface component that extracts/captures photogenerated holes from $BiVO_4$, out-competing intrinsic surface states by providing surface redox states (Co and Fe species), which lie at more favorable energy levels for hole capture from $BiVO_4$, while $CeO_x$ mainly provides an excellent interface quality with $BiVO_4$ for hole transport by passivating the intrinsic surface states of the semiconductor.

Although $Co_{0.4}Fe_{0.1}Ce_{0.5}O_x$ coatings excel at efficient capture and collection of photogenerated holes in $BiVO_4$, the significant differences of the $BiVO_4/Co_{0.4}Fe_{0.1}Ce_{0.5}O_x$ photoanode for $H_2O_2$ and $H_2O$ oxidation suggest that the holes collected by $Co_{0.4}Fe_{0.1}Ce_{0.5}O_x$ cannot be efficiently used for OER, leading to significant surface recombination losses, as shown in Fig. 3. Accordingly, we further assembled $Ni_{0.8}Fe_{0.2}O_x$ catalytic layer on

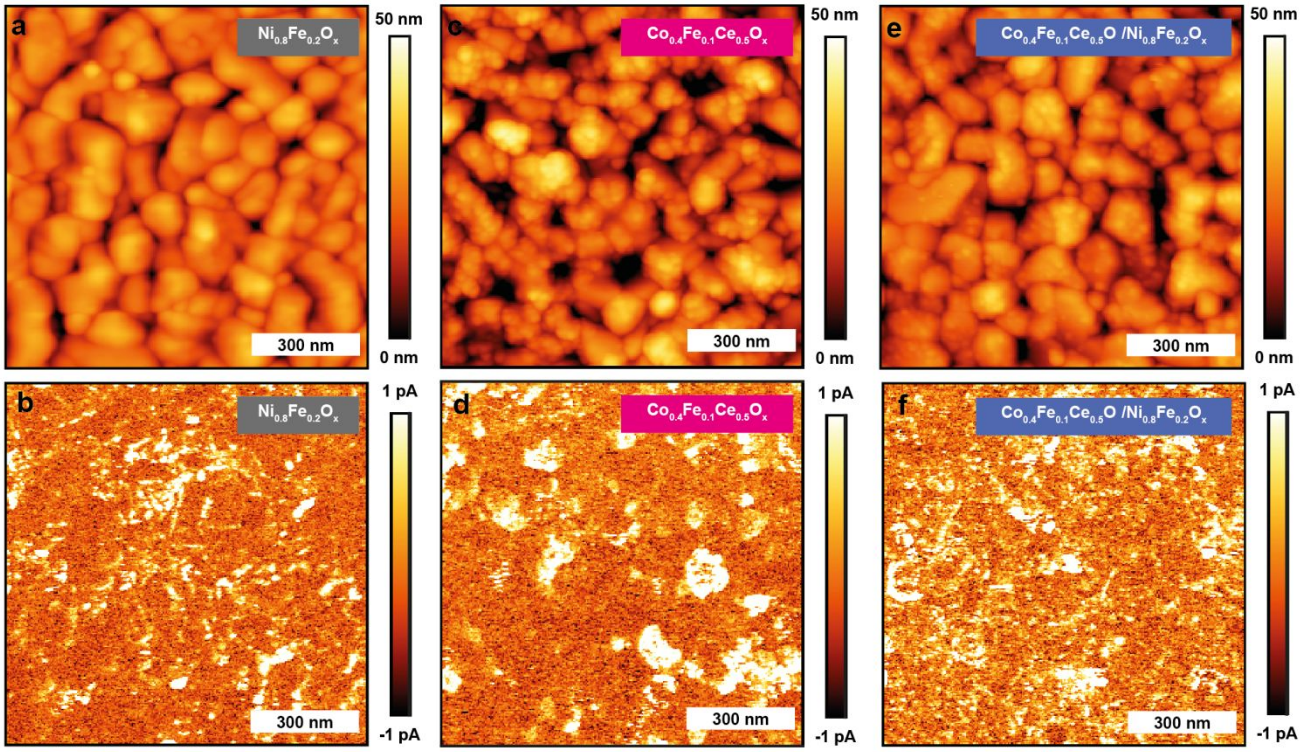

**Figure 4 The pc-AFM measurements.** Topographic and current maps collected for $BiVO_4/Ni_{0.8}Fe_{0.2}O_x$ (**a, b**), $BiVO_4/Co_{0.4}Fe_{0.1}Ce_{0.5}O_x$ (**c, d**), and $BiVO_4/Co_{0.4}Fe_{0.1}Ce_{0.5}O_x$ /$Ni_{0.8}Fe_{0.2}O_x$ (**e, f**).

top of the $BiVO_4/Co_{0.4}Fe_{0.1}Ce_{0.5}O_x$ photoanode, as presented in Fig. S13. As a result, the J-E curve of the $BiVO_4/Co_{0.4}Fe_{0.1}Ce_{0.5}O_x/Ni_{0.8}Fe_{0.2}O_x$ photoanode for OER not only outperforms that of $BiVO_4/Co_{0.4}Fe_{0.1}Ce_{0.5}O_x$ and $BiVO_4/Ni_{0.8}Fe_{0.2}O_x$ but also approaches that for $H_2O_2$ oxidation. Strikingly, 85%-100% of the surface collected holes are used by $Ni_{0.8}Fe_{0.2}O_x$ for OER at 0.8 V-1.23 V vs. RHE, as determined by comparing the J-E curves of $BiVO_4/Co_{0.4}Fe_{0.1}Ce_{0.5}O_x/Ni_{0.8}Fe_{0.2}O_x$ with (dashed line) and without $H_2O_2$ hole scavenger (solid line). This finding demonstrates almost complete elimination of interfacial charge recombination losses with interface optimization. Moreover, PEC performances of the $BiVO_4/Co_{0.4}Fe_{0.1}Ce_{0.5}O_x/Ni_{0.8}Fe_{0.2}O_x$ and $BiVO_4/Co_{0.4}Fe_{0.1}Ce_{0.5}O_x$ photoanodes show similar results with $H_2O_2$. These results demonstrate the addition of $Ni_{0.8}Fe_{0.2}O_x$ greatly improves the interfacial hole transfer of the $BiVO_4/Co_{0.4}Fe_{0.1}Ce_{0.5}O_x$ photoanode for OER without altering its charge separation/transport abilities, whereas $Co_{0.4}Fe_{0.1}Ce_{0.5}O_x$ remedies losses at $BiVO_4/Ni_{0.8}Fe_{0.2}O_x$ interface. To demonstrate generality of our findings, we further performed PEC characterizations of $BiVO_4$, $BiVO_4/Co_{0.4}Fe_{0.1}Ce_{0.5}O_x$ and $BiVO_4/Co_{0.4}Fe_{0.1}Ce_{0.5}O_x/Ni_{0.8}Fe_{0.2}O_x$ at pH 7 (0.1 M KPi), and at pH 9 (0.1 M NaBi)[29]. As a result, the addition of $Co_{0.4}Fe_{0.1}Ce_{0.5}O_x$ and $Co_{0.4}Fe_{0.1}Ce_{0.5}O_x/Ni_{0.8}Fe_{0.2}O_x$ overlayers exhibit similar effect on $BiVO_4$ as in pH 13 electrolyte (Fig. S14)

In order to provide further insights into the charge-transport mechanism through the $BiVO_4/Co_{0.4}Fe_{0.1}Ce_{0.5}O_x/Ni_{0.8}Fe_{0.2}O_x$ interfaces, we investigated the current distributions in $BiVO_4/Ni_{0.8}Fe_{0.2}O_x$, $BiVO_4/Co_{0.4}Fe_{0.1}Ce_{0.5}O_x$, and $BiVO_4/Co_{0.4}Fe_{0.1}Ce_{0.5}O_x/Ni_{0.8}Fe_{0.2}O_x$ by pc-AFM in the dark and under illumination. As shown in Fig. S15 and Fig 4, pc-AFM measurements in the dark at an applied sample bias of 1.75 V reveal bright spots in the current map. We previously observed similar bright spot on pristine $BiVO_4$ and assigned these to shunts between the metal-coated probe and the underling FTO substrate.[30] The photoelectrodeposited catalysts are sparsely distributed on the $BiVO_4$ surface, and preferentially deposited on top of the grains, not on grain boundaries or pinholes, as demonstrated with overlay maps of $BiVO_4/Co_{0.4}Fe_{0.1}Ce_{0.5}O_x$ in Fig. 2a and $BiVO_4/Ni_{0.8}Fe_{0.2}O_x$, $BiVO_4/Co_{0.4}Fe_{0.1}Ce_{0.5}O_x/Ni_{0.8}Fe_{0.2}O_x$ in Fig. S16. Therefore, only a minor role is assigned to a shunt pathway compared to the charge transport across FTO/$BiVO_4$/overlayer.[31]

Furthermore, pc-AFM measurements were also conducted using above band gap illumination ($E_{ph}$ = 3.06 eV, 100 mW/cm²). Maps of the current under illumination (Fig. 4 b, d, f), for the $BiVO_4/Ni_{0.8}Fe_{0.2}O_x$ and the $BiVO_4/Co_{0.4}Fe_{0.1}Ce_{0.5}O_x$ anodes exhibit spots of increased conductivity, whereas an almost homogenous current distribution is observed for the $BiVO_4/Co_{0.4}Fe_{0.1}Ce_{0.5}O_x/Ni_{0.8}Fe_{0.2}O_x$ anode. In all three samples, under illumination the current mainly increases on top of the grain and not at the grain boundaries. The corresponding median photocurrents are 0.08 pA for $BiVO_4/Ni_{0.8}Fe_{0.2}O_x$, 0.28 pA for $BiVO_4/Co_{0.4}Fe_{0.1}Ce_{0.5}O_x$, and 0.38 pA for $BiVO_4/Co_{0.4}Fe_{0.1}Ce_{0.5}O_x/Ni_{0.8}Fe_{0.2}O_x$. These findings are in agreement with the PEC measurements presented above, which showed improved performance for $BiVO_4/Co_{0.4}Fe_{0.1}Ce_{0.5}O_x/Ni_{0.8}Fe_{0.2}O_x$. The higher photocurrent value of $BiVO_4/Co_{0.4}Fe_{0.1}Ce_{0.5}O_x$ compared to $BiVO_4/Ni_{0.8}Fe_{0.2}O_x$ might indicate that hole extraction/collection from $BiVO_4$ is more feasible *via* the $Co_{0.4}Fe_{0.1}Ce_{0.5}O_x$ overlayer. Accordingly, the photo-conductivity of $BiVO_4/Ni_{0.8}Fe_{0.2}O_x$ is greatly enhanced once $Co_{0.4}Fe_{0.1}Ce_{0.5}O_x$ is inserted between $Ni_{0.8}Fe_{0.2}O_x$ and $BiVO_4$. These results not only confirm the role of $Co_{0.4}Fe_{0.1}Ce_{0.5}O_x$ as a hole mediator/collector, but also verify that the holes collected by $Co_{0.4}Fe_{0.1}Ce_{0.5}O_x$ can be efficiently used by $Ni_{0.8}Fe_{0.2}O_x$ to drive the OER.

## 3. Conclusions

In summary, we have investigated the critical interfacial roles of individual component metal oxides in the $(NiFeCoCe)O_x$ multi-component overlayers by interfacing each of them with $BiVO_4$. We have identified $(NiFe)O_x$ as the surface catalytic component and $(CoFeCe)O_x$ as the charge capture/collection component *via* available redox active states, by using PEC characterizations with and without a $H_2O_2$ hole scavenger. The charge capture/collection mechanism of $(CoFeCe)O_x$ from $BiVO_4$ was also studied in detail with OCP and TPC measurements. Accordingly, we further optimized $BiVO_4/(NiFeCoCe)O_x$ by serially interfacing the $(CoFeCe)O_x$ hole collector and $(NiFe)O_x$ catalyst with $BiVO_4$. In addition, our findings corroborate that $BiVO_4$ surface trap states may be catalytically active for OER catalysis. The resulting integrated photoanode almost eliminates interfacial losses across the $BiVO_4$/electrolyte interface over the range of 0.8-1.23 V vs. RHE for OER. The effective charge transfer through the $(CoFeCe)O_x$ hole collector and $(NiFe)O_x$ catalyst interfaces was further verified by pc-AFM measurements. This study highlights the roles of $(NiFeCoCe)O_x$ multi-component overlayers in preferentially capturing holes over the surface states of $BiVO_4$ as well as catalyzing the OER. This work demonstrates the significance of interface optimization in the multi-component overlayer-integrated $BiVO_4$ photoanodes, establishing foundational knowledge to design the next generation of integrated photo-active materials for solar fuels production.

## 4. Experimental

### 4.1 Fabrication of $BiVO_4$ films

Spin-coated bismuth vanadate ($BiVO_4$) thin films were deposited on the fluorine-doped tin oxide (FTO)-coated side of a 10 cm × 10 cm glass plate (TEC-15 Sigma Aldrich), following a procedure from our previous report.[11] FTO/glass substrates were thoroughly washed with isopropanol (Sigma Aldrich, ⩾ 98%), detergent (Alconex) in deionized water, and pure deionized water, dried with a nitrogen gun and treated with an ozone cleaner (Jelight Model 42) for 10 min.

For spin coating, typically, 15 mL of a 0.2 M solution of bismuth (III) nitrate pentahydrate (Sigma Aldrich, ⩾ 98%) in acetylacetone (Sigma Aldrich, ⩾99%) and 100 mL of a 0.03 M solution of vanadium (IV)-oxyacetylacetonate in acetylacetone were prepared separately and sonicated for 10 min. Then, the two solutions were mixed together and further sonicated for 5 min. The resulting solution was filtered with 0.45 µm nylon filters (Thermo Fisher Scientific), and dispensed onto the 10 cm × 10 cm FTO/glass plate. The substrate was then spun two times at 1000 rpm for 6 s on a spin coater (Laurell Technologies) with an acceleration rate of 150 rpm/s and annealed in air for 10 min at 500 °C in a muffle furnace (Cole-Parmer). This spin coating-annealing procedure was repeated nine times. After the last spin coating cycle, the substrate was annealed for 2 h at 500 °C to yield a final thickness of ~50 nm.

### 4.2 Photoelectrochemical deposition (PED) of catalysts

Catalysts were produced via PED on $BiVO_4$ electrodes. 0.1 M solution of various metal nitrates (nickel (II) nitrate hexahydrate, Sigma Aldrich, ⩾ 97%; iron nitrate (III) nonahydrate Sigma Aldrich, ⩾98%; cobalt (II) nitrate hexahydrate, Strem chemicals, ⩾99%; cerium nitrate (III) hexahydrate, Sigma Aldrich, ⩾99%) was used as an electrolyte. PED was conducted in an undivided cell at a constant current density of 50 $\mu A\ cm^{-2}$ over a period of 60 min under AM 1.5G-simulated sunlight. The $BiVO_4$ electrode was used as the working electrode, Ag/AgCl as the reference electrode and a Pt wire as the counter electrode. The light irradiation came from the back side of electrodes. The precursor solution of $(CoFeCe)O_x$ was prepared by mixing 0.08 M cobalt (II) nitrate hexahydrate, 0.01 M iron nitrate (III) nonahydrate and 0.01 M cerium nitrate (III) hexahydrate into in total 0.1 M metal nitrate solution. Likewise, the precursor solution of $(NiFe)O_x$ was prepared by mixing 0.08 M nickel (II) nitrate hexahydrate, 0.02 M iron nitrate (III) nonahydrate into in total 0.1 M metal nitrate solution.The reported ratios in the chemical formulas were provided by ICP-MS results. $BiVO_4/Co_{0.4}Fe_{0.1}Ce_{0.5}O_x/Ni_{0.8}Fe_{0.2}O_x$ sample was assembled by depositing $Co_{0.4}Fe_{0.1}Ce_{0.5}O_x$ for 15 min and then $Ni_{0.8}Fe_{0.2}O_x$ for the rest 45 min.

### 4.3 UV-Vis Transmission and Reflectance Measurements

Transmission and spectral reflectance measurements were performed on a Shimadzu SolidSpec-3700 UV/Vis/NIR spectrometer using an integrating sphere.

### 4.4 Photoelectrochemical (PEC) and Open circuit potential (OCP) measurements

The PEC test was conducted in a single-compartment, three-electrode electrochemical cell with a potentiostat (Bio-Logic, SP-300) under simulated AM 1.5G solar light irradiation (100 mWcm$^{-2}$, 16S-300-002, Solar Light). The fabricated electrode, a platinum wire, and Ag/AgCl electrode were used as working, counter, and reference electrodes, respectively. Unless expressly mentioned, 0.1 M NaOH aqueous solution (pH = 13) was used as an electrolyte after saturation with $N_2$ gas for 20 min. The measured potentials were converted to V vs. RHE ($E_{RHE} = E_{Ag/AgCl} + 0.193\ V + 0.059\ V \times pH$). The photocurrent was measured by linear sweep voltammetery with a scan rate of 10 mV s$^{-1}$. The light irradiation came from the front side of electrodes for all cases. OCP measurements were performed under open circuit condition in the same electrolyte. OCP reading in dark or under illumination was obtained after a stabilization process in dark (10 min)

### 4.5 Transient photocurrent (TPC) measurements

TPC measurements were conducted in a similar setup to PEC measurements. The main difference is the working electrode was exposed to a continuous ~ 100 mWcm$^{-2}$ light bias from a home-built white light-emitting diode (LED) array. A 340 nm LED (M340L4, ThorLabs) with ~10 nm spectral full width at half maximum (FWHM) and ~ 10 mW cm$^{-2}$ power density was used as the modulating light source, alternating between 150 ms on-time and 203 ms off-time. The applied potential was increased from 0.56 to 1.36 V vs. RHE at 0.05 V intervals. After passing through a current pre-amplifier (SR570, Stanford Research Systems), the photocurrent transients induced by the 340 nm LED were collected at a frequency of $10^5$ Hz and averaged over 100 light pulses.

### 4.6 X-ray photoelectron spectroscopy (XPS) and Inductively coupled plasma mass spectrometry (ICP-MS)

The near-surface chemical composition was analyzed by XPS using a monochromatized Al K$\alpha$ source ($h\nu = 1486.6\ \mathrm{eV}$) on a Kratos Axis Ultra DLD system with a pass energy of 20 eV. Spectral fitting was conducted using Casa XPS analysis software. Spectral energy positions were corrected by shifting the C 1s core level position to 284.8 eV and curves were fit with quasi-Voigt lines following Shirley background subtraction. ICP-MS was performed using an Agilent 7900 system run using the He mode. The internal standard was Ge for Ni, Fe, Co and Tb for Ce, selected based on their first ionization potentials and M/Z. Samples were digested with 1 mL of 70% $HNO_3$ (>99.999% trace metals basis, 225711, Aldrich) and diluted into 5 mL in total with 1% $HNO_3$ solution as the original sample solutions

### 4.7 Transmission electron microscopy (TEM) measurements

TEM measurements were conducted on a FEI TitanX 60-300 microscope at NCEM using a double tilt holder and an accelerating voltage of 200 kV. Images were acquired with a HAADF detector for STEM. EDS was collected using a Bruker windowless EDS detector.

### 4.8 Atomic force microscopy (AFM) measurements

All AFM measurements were performed with a commercial AFM system (Bruker Dimension Icon). PeakForce Quantitative Nanoscale Mechanical (PF-QNM) mode was used for recording topography and adhesion maps simultaneously. For all PF-QNM measurements, uncoated Si-probes (RFESP-75) with spring constants of 3.0 N m$^{-1}$ were used.

For pc-AFM mapping, PeakForce TUNA mode was used, whereby a positive bias of 1.75 V was applied to the FTO back contact. For all pc-AFM measurements, the sample was illuminated from the FTO-side using a specially designed illumination setup.[30] As light source, a CW laser diode with wavelength of 405 nm and an illumination intensity of about 100 mW cm$^{-1}$ was used. Pc-AFM measurements were performed with conductive PtIr-coated probes (Bruker SCM-PIT) exhibiting a nominal spring constant of 2.8 N m$^{-1}$.

## Conflicts of interest

There are no conflicts to declare.

## Acknowledgements

This study is based on work performed at the Joint Center for Artificial Photosynthesis, a DOE Energy Innovation Hub, supported through the Office of Science of the U.S. Department of Energy under Award Number DE-SC0004993. Work at the Molecular Foundry was supported by the Office of Science, Office of Basic Energy Sciences, of the U.S. Department of Energy under Contract No. DE-AC02-05CH11231.

## Notes and references

1. J. Su and L. Vayssieres, *ACS Energy Letters*, 2016, **1**, 121-135.
2. N. S. Lewis, *Science*, 2007, **315**, 798-801.
3. S. Dahl and I. Chorkendorff, *Nat Mater*, 2012, **11**, 100-101.
4. M. Gratzel, *Nature*, 2001, **414**, 338-344.
5. M. G. Walter, E. L. Warren, J. R. McKone, S. W. Boettcher, Q. Mi, E. A. Santori and N. S. Lewis, *Chemical Reviews*, 2010, **110**, 6446-6473.
6. X. Chen, C. Li, M. Gratzel, R. Kostecki and S. S. Mao, *Chemical Society Reviews*, 2012, **41**, 7909-7937.
7. B. A. Pinaud, J. D. Benck, L. C. Seitz, A. J. Forman, Z. Chen, T. G. Deutsch, B. D. James, K. N. Baum, G. N. Baum, S. Ardo, H. Wang, E. Miller and T. F. Jaramillo, *Energy & Environmental Science*, 2013, **6**, 1983-2002.
8. I. D. Sharp, J. K. Cooper, F. M. Toma and R. Buonsanti, *ACS Energy Letters*, 2017, **2**, 139-150.
9. F. F. Abdi, T. J. Savenije, M. M. May, B. Dam and R. van de Krol, *The Journal of Physical Chemistry Letters*, 2013, **4**, 2752-2757.
10. B. Pattengale and J. Huang, *Physical Chemistry Chemical Physics*, 2017, **19**, 6831-6837.
11. F. M. Toma, J. K. Cooper, V. Kunzelmann, M. T. McDowell, J. Yu, D. M. Larson, N. J. Borys, C. Abelyan, J. W. Beeman and K. M. Yu, *Nature Communications*, 2016, **7**.

12. H. Ye, H. S. Park and A. J. Bard, *The Journal of Physical Chemistry C*, 2011, **115**, 12464-12470.
13. D. K. Zhong, S. Choi and D. R. Gamelin, *Journal of the American Chemical Society*, 2011, **133**, 18370-18377.
14. C. Ding, J. Shi, D. Wang, Z. Wang, N. Wang, G. Liu, F. Xiong and C. Li, *Physical Chemistry Chemical Physics*, 2013, **15**, 4589-4595.
15. J. A. Seabold and K.-S. Choi, *Journal of the American Chemical Society*, 2012, **134**, 2186-2192.
16. T. W. Kim and K. S. Choi, *Science*, 2014, **343**, 990-994.
17. M. Zhong, T. Hisatomi, Y. Kuang, J. Zhao, M. Liu, A. Iwase, Q. Jia, H. Nishiyama, T. Minegishi, M. Nakabayashi, N. Shibata, R. Niishiro, C. Katayama, H. Shibano, M. Katayama, A. Kudo, T. Yamada and K. Domen, *Journal of the American Chemical Society*, 2015, **137**, 5053-5060.
18. D. Guevarra, A. Shinde, S. K. Suram, I. D. Sharp, F. M. Toma, J. A. Haber and J. M. Gregoire, *Energy & Environmental Science*, 2016, **9**, 565-580.
19. A. Shinde, D. Guevarra, G. Liu, I. D. Sharp, F. M. Toma, J. M. Gregoire and J. A. Haber, *ACS Applied Materials & Interfaces*, 2016, **8**, 23696-23705.
20. C. Zachaus, F. F. Abdi, L. M. Peter and R. van de Krol, *Chemical Science*, 2017, **8**, 3712-3719.
21. G. V. Govindaraju, G. P. Wheeler, D. Lee and K.-S. Choi, *Chemistry of Materials*, 2017, **29**, 355-370.
22. J. A. Haber, E. Anzenburg, J. Yano, C. Kisielowski and J. M. Gregoire, *Advanced Energy Materials*, 2015, **5**, 1402307.
23. A. Shinde, G. Li, L. Zhou, D. Guevarra, S. K. Suram, F. M. Toma, Q. Yan, J. A. Haber, J. B. Neaton and J. M. Gregoire, *Journal of Materials Chemistry A*, 2016, **4**, 14356-14363.
24. J. M. Spurgeon, J. M. Velazquez and M. T. McDowell, *Physical Chemistry Chemical Physics*, 2014, **16**, 3623-3631.
25. B. J. Trzesniewski and W. A. Smith, *Journal of Materials Chemistry A*, 2016, **4**, 2919-2926.
26. F. Le Formal, K. Sivula and M. Grätzel, *The Journal of Physical Chemistry C*, 2012, **116**, 26707-26720.
27. F. A. L. Laskowski, J. Qiu, M. R. Nellist, S. Z. Oener, A. M. Gordon and S. Boettcher, *Sustainable Energy & Fuels*, 2018.
28. G. Liu, J. Shi, F. Zhang, Z. Chen, J. Han, C. Ding, S. Chen, Z. Wang, H. Han and C. Li, *Angewandte Chemie International Edition*, 2014, **53**, 7295-7299.
29. L. Zhou, A. Shinde, D. Guevarra, F. M. Toma, H. S. Stein, J. M. Gregoire and J. A. Haber, *ACS Applied Energy Materials*, 2018.
30. J. Eichhorn, C. Kastl, J. K. Cooper, D. Ziegler, A. M. Schwartzberg, I. D. Sharp and F. M. Toma, *Nature Communications*, 2018, **9**, 2597.
31. J. Qiu, H. Hajibabaei, M. R. Nellist, F. A. L. Laskowski, S. Z. Oener, T. W. Hamann and S. W. Boettcher, *ACS Energy Letters*, 2018, **3**, 961-969.

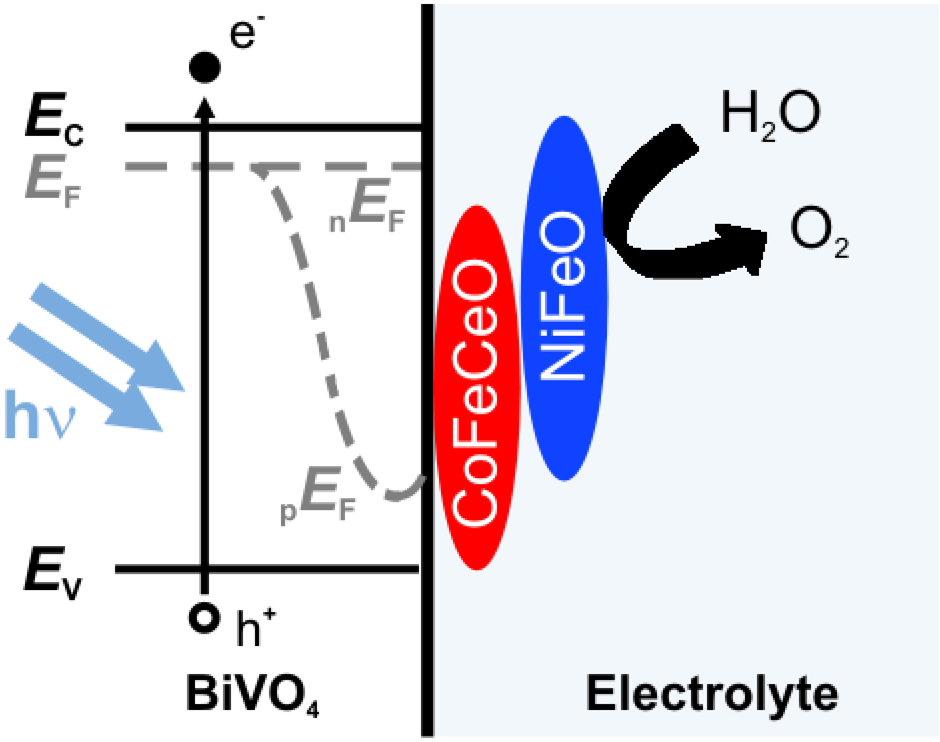

39x31mm (300 x 300 DPI)